Defect Detection in Solid-State Battery Electrolytes Using Lock-In Thermal Imaging

Dana B. Sulas, [1,z] Steve Johnston,[1] Natalie Seitzman,[1,2,*] Heather Platt,[3] Mowafak Al-Jassim,[1] and Harvey Guthrey[1]

[1] *National Renewable Energy Laboratory, Golden, Colorado 80401, USA*
[2] *Colorado School of Mines, Golden, Colorado 90401, USA*
[3] *Solid Power, Louisville, Colorado 80027, USA*

Defective regions in battery materials often generate excess or non-uniform heat profiles during operation. Here, we discuss lock-in thermography as a high-sensitivity, spatially-resolved, and non-destructive technique to characterize defects and guide the targeted optimization of new battery materials and cell designs. As an example, we thermally image all-solid-state cells with β-Li$_3$PS$_4$ electrolyte, showing point-like heat signatures that correlate with cell breakdown. Based on the current/voltage cycling characteristics and electrochemical impedance spectroscopy, we attribute heating at the breakdown sites primarily to resistive current flow through dendrites. To assist in enabling wider application of lock-in thermography to emerging battery materials, we discuss several parameters necessary to optimize this technique, including the influences of surface thermal emissivity, thermal diffusivity, and lock-in modulation frequency.

With increasing electric vehicle deployment and need to store energy from renewable sources, the demand continues to rise for large battery systems with high energy densities and fast charge/discharge rates. All-solid-state batteries have emerged with the promise of relative mechanical and chemical stability, offering increased resilience toward thermal problems and dendrite formation, as well as a possibility to use high-energy-density lithium-metal electrodes.[1,2] However, commercialization of this technology is lacking, in part due to inadequate understanding of defect evolution and the impact of defects on device safety and lifetime.[2]

Defects may be detected during battery operation by spatial characterization of heat dissipation, informing the targeted optimization of emerging electrochemical materials and cell designs. Heat generation in battery systems is undesirable but unavoidable, resulting from both exothermic chemical reactions and resistive current flow.[3,4] Temperature nonuniformities, which may indicate changes in the battery's local chemical composition, electrode/electrolyte integrity, or packaging, may evolve following stresses such as continued charge/discharge cycling, external heating, overcharging, or mechanical impact.[3,5,6] Locating areas of excessive or nonuniform heat generation can pinpoint sites that may accelerate degradation or (in liquid electrolyte systems) trigger dangerous thermal runaway.[5,6]

The numbers of both computational and experimental electrical-thermal characterization methods for battery systems have been rapidly growing, although several challenges still remain.[7–16] Numerical models continue to increase in sophistication, but accurate results rely on detailed knowledge of the cell and materials properties for input parameters.[7,13,17] This challenge is addressed to some extent by combining computational and experimental methods, where parameters such as the cell's average surface temperature, coolant temperature, current, voltage, and impedance are continually monitored and fed back into the calculation.[9–12]

Experimentally, surface-mounted and embedded sensors provide direct temperature measurements, sometimes with spatial information if multiple sensors are employed.[13,14,18,19] However, using physically-mounted sensors presents practical difficulties that become more pronounced with increasing size of the battery system. For example, retrofitting batteries with embedded sensors is often destructive,[13] so structurally and chemically compatible sensors are ideally incorporated during cell fabrication.[14] Although surface sensors are more easily applied, the number of sensors required to obtain spatial resolution or to probe every cell within a large battery pack may rapidly

become costly and time consuming. For these reasons, sensorless methods such as electrochemical impedance have gained popularity for estimating internal temperature.[10,15,16] However, impedance spectroscopy is a bulk method and does not provide spatial information about temperature nonuniformities.

Thermal imaging with infrared cameras is a promising, non-destructive method for obtaining spatially-resolved heating information during battery operation without using sensors or needing to develop complicated thermal models.[6,17,20–22] Here, we discuss a high-sensitivity variant of thermal imaging in which we use lock-in amplification to detect nonuniformities in heat dissipation from β-Li$_3$PS$_4$ solid-state electrolyte cells with symmetric lithium electrodes. By referencing the thermal measurement to the temporal frequency of an oscillating current stimulus, we image electrically-induced heating while avoiding noise from the steady-state temperature background. Using the lock-in technique, we are able to measure heating with as little as 1.8 mA/cm^2 current densities. We further discuss the unique benefits of lock-in thermography for imaging battery systems, and we provide insight for optimal experimental design. As an example, we apply lock-in thermography to identify defective areas after critical breakdown following increasing current cycling of the Li/β-Li$_3$PS$_4$/Li cells. Interestingly, we observe distinct, point-like heat signatures after cell breakdown. Based on the equivalent circuit derived from impedance analysis, we attribute the heating to resistive current flow through dendrites. Guided by the thermal images, we improve our cell design by identifying weak areas around the cell perimeter that correlate with dendrite growth.

Experimental

Materials.—We fabricated symmetric Li/β-Li$_3$PS$_4$/Li cells in an inert glove box environment by compressing β-Li$_3$PS$_4$ powder at 6 metric tons in a 1.6 cm diameter die composed of electrically insulating polyaryletheretherketone (PEEK). The β-Li$_3$PS$_4$ powder was prepared by Solid Power. After the β-Li$_3$PS$_4$ pellets were prepared, Li metal disks (MTI) were attached to both surfaces of each pellet by pressing at 0.5 metric tons.

Thermal imaging.—Figure 1a shows the design of our sample chamber for thermal imaging of Li/β-Li$_3$PS$_4$/Li cells. We contact the bottom Li electrode with a steel post, and we contact the top Li electrode using a steel foil coated with black spray paint. We further discuss the role of black paint to increase and homogenize thermal emissivity in lock-in thermal imaging of defect sites section of the Results and Discussion. We compress the sample to ensure good
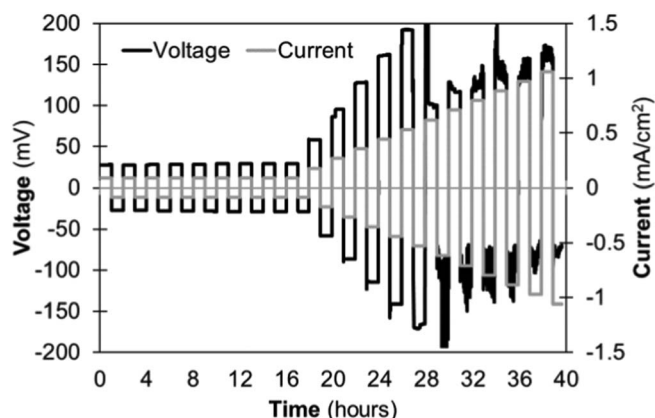
*Electrochemical Society Student Member.
zE-mail: dana.sulas@nrel.gov
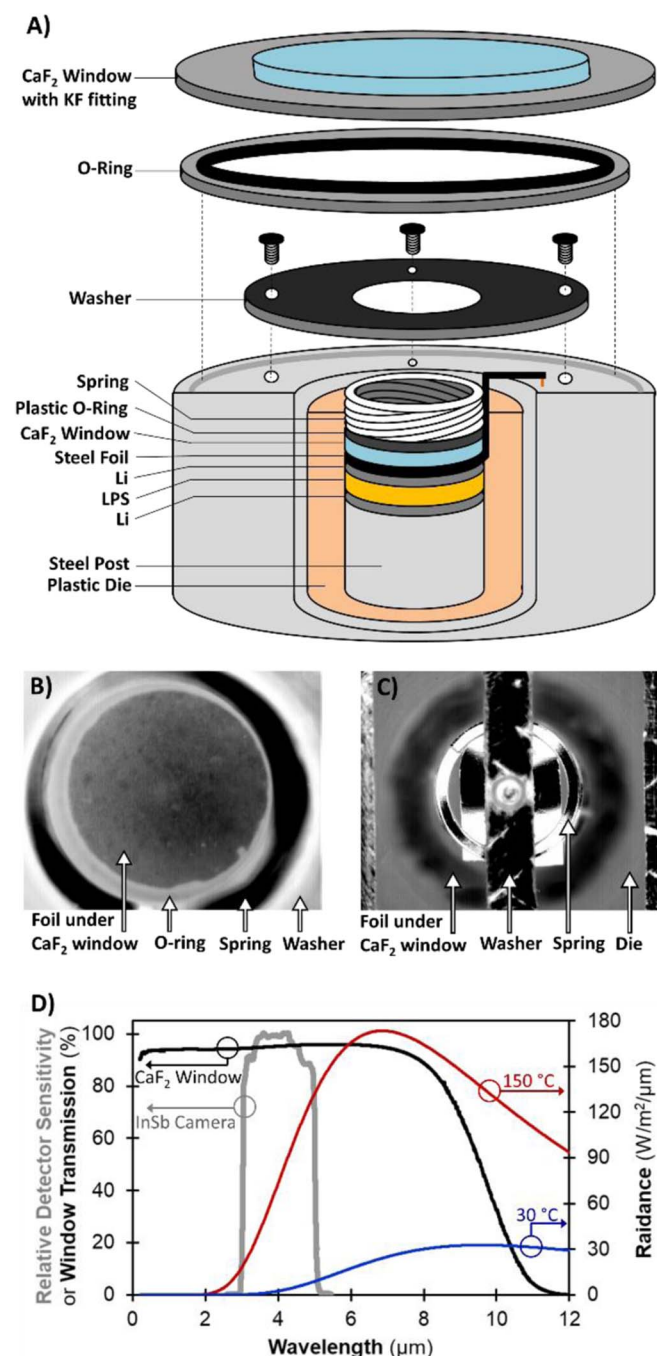
Figure 1. (a) Schematic diagram of the sample chamber for thermal imaging (not to scale) along with (b-c) steady-state images from the camera's point of view for different spring/washer assemblies used for imaging (b) the sample center or (c) the sample edge. (d) Transmission of CaF$_2$ windows overlaid with the relative detector sensitivity of an InSb camera, showing sufficient spectral overlap of our detection system with blackbody radiance in the typical temperature range for Li-ion battery operation (plotted using Planck's law).

Figure 2. Representative cycling data for a symmetric Li/β-Li$_3$PS$_4$/Li cell showing critical breakdown around 0.62 mA/cm^2.

The cell remains air-free in a sealed chamber loaded under argon atmosphere, and we perform thermal imaging through CaF$_2$ windows that are heat-transmissive in the 0.1–10 µm range. Figure 1d shows that the CaF$_2$ windows have high transmission over the entire detectivity range (3–5 µm) of our cooled FLIR SC5000MB InSb infrared camera. In addition, our camera has sufficient spectral overlap with the radiance of black bodies in the typical temperature range of Li ion battery operation. Figure 1d illustrates that, as the temperature of the sample increases during cycling, the intensity of thermal radiation increases and the peak radiance shifts to shorter wavelengths (toward the camera's highest detectivity range).

We image the heat signatures using lock-in amplification, and we report the total signal ($r = \sqrt{x^2 + y^2}$) including both in-phase (x = V_{sig} cosθ) and quadrature (y = V_{sig} sinθ), where V_{sig} is the signal amplitude and θ is the phase shift. Reporting r removes the phase dependence from the final image, which is necessary when the built-in phase shift inherent to the electronics is uncalibrated. We record our data using FLIR's Altair and Thesa software. We modulate the current from 0 A to the maximum current as indicated in the respective figures, and we further elaborate on the factors that influence our choice of modulation frequency in lock-in thermal imaging of defect sites section of the Results and Discussion.
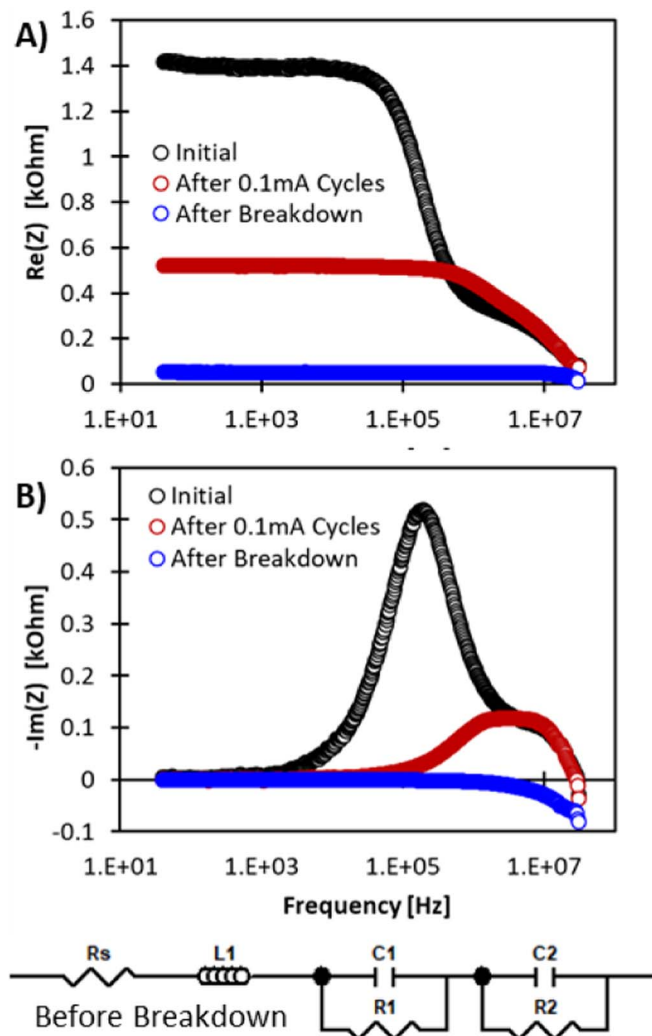
We perform a rough calibration of the thermal detector counts as described by Breitenstein et al.,[23] in which we resistively heat a black-painted strip of copper metal while simultaneously recording its change in temperature over the modulation period. We plot the detector counts against the modulated temperature difference in the range of 0.1–1 K, and we extrapolate peak temperature modulation in the range of 60–80 mK for the Li/ β-Li$_3$PS$_4$/Li thermal images.

Impedance analysis.—We record impedance data with an Agilent 4294A precision impedance analyzer over 40 Hz to 30 MHz with 0 V DC bias and 5 mV AC bias. We fit our data using Zview software.

Cycling.—We source current and measure voltage in 1-hour cycles with data points every ∼12 seconds using a Keithley 2401 sourcemeter.

Results and Discussion

Critical breakdown of Li/β-Li$_3$PS$_4$/Li cells.—To evaluate the effectiveness of thermal imaging for locating defect sites, we first induce short-circuit defects by cycling the Li/β-Li$_3$PS$_4$/Li cells under increasing current densities until breakdown occurs. Figure 2 shows representative cycling data. The cells are stable for an extended period of time under +/− 0.09 mA/cm^2. After increasing the current magnitude by 0.09 mA/cm^2 for each cycle, we observe critical breakdown at the +/− 0.62 mA/cm^2 cycle, which is within the 0.4–1 mA/cm^2

contact of the electrodes and to restrict volume changes during cycling. Without confining pressure, the electrodes tend to delaminate from the β-Li$_3$PS$_4$ electrolyte. We apply even pressure to the sample surface using a calcium fluoride (CaF$_2$) window that is pressed by a spring/o-ring assembly underneath a washer. In Figures 1b–1c, we show the steady-state view of the sample from the camera's perspective. We use two different geometries for the washer/spring/o-ring assembly to image the sample's center (Figure 1b) and edges (Figure 1c).

Figure 3. Impedance data for a symmetric Li/β-Li$_3$PS$_4$/Li cell before cycling (black), after +/− 0.09 mA/cm^2 cycles (red), and after critical breakdown (blue) showing (a) the real impedance component (Re(Z)) and (b) the imaginary impedance component (-Im(Z)) over a range of frequencies from 40 Hz to 30 MHz along with the equivalent circuit that best fits our data.

range that breakdown typically occurs in similar materials.[24–26] Critical breakdown is characterized by an abrupt drop in voltage, which indicates increased conductivity though short-circuit defects. Such short-circuit defects are commonly referred to as dendrites, and we retain this terminology in our study. However, due to the porous electrolyte microstructure, the defects should be interpreted more generally as features formed by lithium metal propagation and not as fractal tree-like structures associated with dendrite growth in uniform media. We note that solid-state electrolytes such as β-Li$_3$PS$_4$ are promising for their resilience against dendrite formation compared to liquid electrolyte cells, though some dendrites may nevertheless form when stressing to the point of breakdown because of lithium movement into cracks, pores, or grain boundaries.[24,27]

We further characterize the cell's electrical properties before and after breakdown using impedance spectroscopy, showing a change in the cell's response from a capacitive to an inductive equivalent circuit. We interpret these results as confirmation that cell failure is likely caused by shorting through dendrites.

Figures 3a and 3b show the real (Re) and imaginary (Im) parts, respectively, of the impedance amplitude (Z) over a range of frequencies from 40 Hz to 30 MHz. Before cycling, the cell initially shows high Re(Z) around 1.4 kΩ at lower frequencies with a strong negative slope around 0.1 MHz followed by a second feature at high frequency

>1 MHz. The two locations of negative slope (∼0.1 and 10 MHz) represent two resistor-capacitor (RC) time constants, which are mirrored as two peaks in -Im(Z) versus frequency (Figure 3b). We provide the equivalent circuit that fits our data in Figure 3. We attribute the lower frequency RC component to charge-transfer resistance, and we attribute the higher frequency component to the bulk β-Li$_3$PS$_4$.[28]

After stable cycling for about 20 hours at +/− 0.09 mA/cm^2, we observe a decrease in Re(Z) from 1.4 kΩ to 0.58 kΩ at low frequency (Figure 3a). We attribute this decrease to conditioning of the Li/β-Li$_3$PS$_4$ interfaces, which decreases the charge-transfer resistance. The decrease in charge-transfer resistance is reflected in Figure 3b as suppression of the lower frequency -Im(Z) peak and its shift from about 0.2 to 2 MHz. We note that two RC components still remain following the +/− 0.09 mA/cm^2 cycling, visible as two peaks in -Im(Z). The high frequency component appears to be unchanged following +/− 0.09 mA/cm^2 cycling, indicating that the bulk β-Li$_3$PS$_4$ remains intact and the main change is interface conditioning.

After critical breakdown (corresponding to the abrupt voltage drop in Figure 2), our impedance results in Figure 3 indicate that the sample has become a low-resistance inductor, consistent with dendrite formation. The decrease in Re(Z) across all frequencies indicates high conductance through the cell. Additionally, the opposite sign of -Im(Z) compared to pre-breakdown is characteristic of the positive phase shift expected for inductive circuits.

Lock-in thermal imaging of defect sites.—Next, we use lock-in thermal imaging to locate the defect sites after cell breakdown. We show that cell breakdown correlates with distinct point-like heat signatures, which we attribute to resistive heating at dendrites. Importantly, we note that lock-in thermography is sensitive to very small amounts of heat dissipation, and we estimate the modulated temperature at the short-circuit defects in the range of 60–80 mK under our measurement conditions. In this section, we further discuss factors that influence the measurement sensitivity and resolution, including surface thermal emissivity, thermal diffusivity, and modulation frequency.

In Figure 4, we show that using a black-painted steel foil top contact improves detection of distinct hot spots by ensuring uniform and high thermal emissivity (ε) across the sample surface. Compared to a wire contact, our black foil contact reduces artifacts due to material-dependent ε values that can vary with wavelength, temperature, surface roughness, and viewing angle.[23]

In Figures 4a–4d, we compare images of the same post-stress cell with either a black-painted steel foil top contact (Figures 4a–4b) or a wire contact embedded in the lithium metal (Figures 4c–4d), each at two different current modulation frequencies (2 or 0.2 Hz) with 4.4 mA/cm^2 amplitude. With the steel foil contact, we observe heat dissipation from two distinct points, which we attribute to heating at the dendrites. However, with the wire contact we are unable to detect distinct points of heat dissipation. Instead, the thermal images in Figures 4c–4d are dominated by artifacts that correlate with visible texture variations across the lithium surface. In addition, the maximum signal magnitude that we measure with the wire contact is lower compared to the measurement with the foil contact. We attribute the lower signal magnitude to lower thermal emissivity for metal surfaces (ε ∼ 0.03–0.3) compared to black painted surfaces (ε ∼ 0.96).[23] The low ε and the texture variations with the wire contact mask defect heat signatures, so we use the steel foil contact in our following analysis to identify breakdown defects.
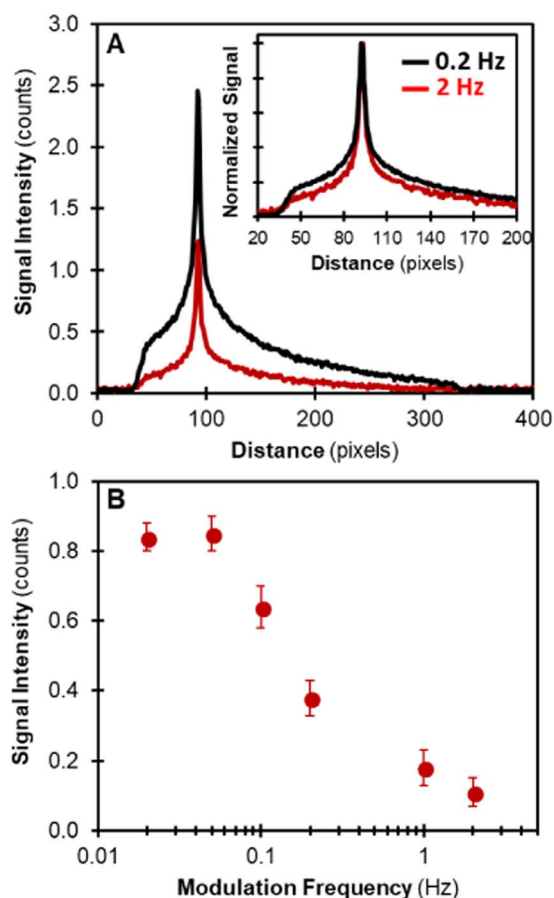
In Figures 4e–4f, we show a control measurement of our sample holder in short circuit with the foil contacting the metal post. These control results show that the heat signatures in Figures 4a–4b are indeed related to the Li/β-Li$_3$PS$_4$/Li sample and not artifacts caused by the foil contact method. In the short-circuit sample holder, we observe minimal heating with 50 mA/cm^2 at 0.2 Hz (Figure 4e), and we see a small amount of heat near the foil's contact pin with 150 mA/cm^2 at 0.2 Hz (Figure 4f). The weak, diffuse heat profile in the control is dissimilar to the distinct point-like defects that we observe upon cell breakdown in Figures 4a–4b. In addition, the maximum signal magnitude in the Li/β-Li$_3$PS$_4$/Li cells is ∼10 times higher compared
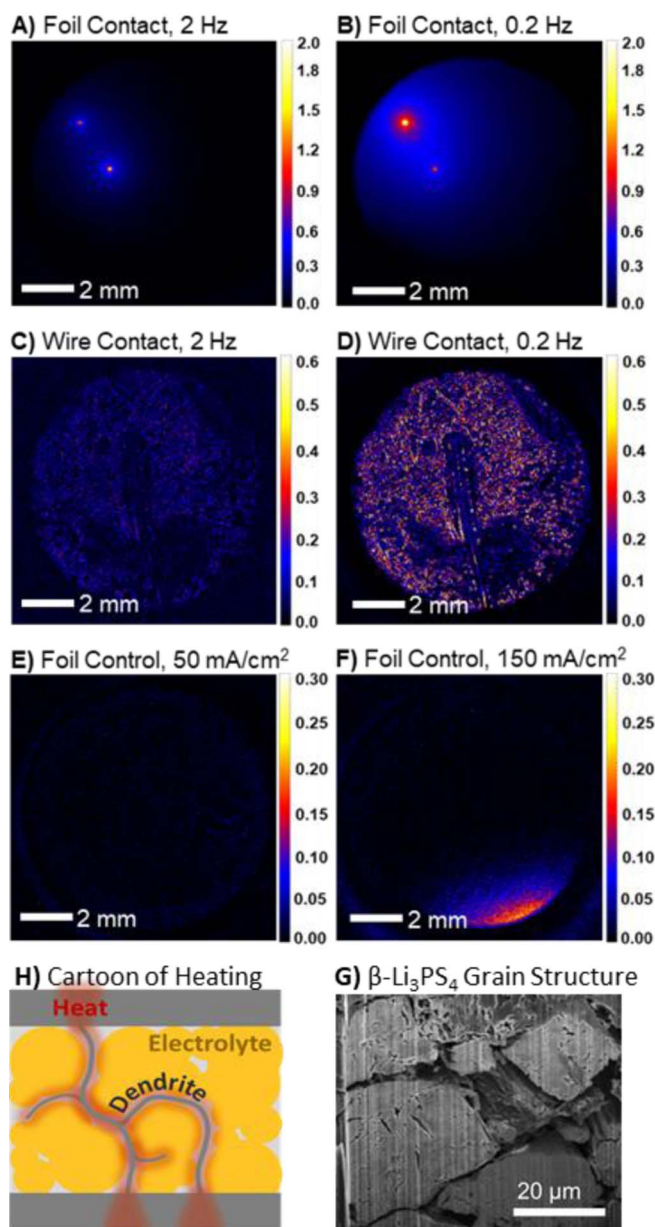
Figure 4. Thermal images on the same Li/β-Li$_3$PS$_4$/Li cell collected using a top contact made of (a-b) steel foil painted in matte black, or (c-d) steel wire. Images were collected using lock-in detection referenced to a current modulated at (a,c) 2 Hz or (b,d) 0.2 Hz at max amplitude of 4.4 mA/cm^2. Control measurement (e-f) with foil contact shorting the sample holder shows minimal signal at 0.2 Hz and maximum amplitude of (e) 50 mA/cm^2 or (f) 150 mA/cm^2. Cells in (a-d) are imaged with the edge-spring assembly (see Figure 1c) and have 1.5 cm^2 Li electrodes that do not contact the edges of the palletization die. Intensity scale is given as detector counts. Cartoon (h) illustrates possibility of extended dendrite structure larger than the point of detected heat, supported by (g) scanning electron microscopy image of electrolyte grain structure with pores extending 10's to 100's of micrometers.

Figure 5. (a) Intensity profiles for line scans through the upper left defect in Figures 4a–4c for the 0.2 Hz (black) and 2 Hz (red) measurements, showing higher signal intensity for the slower modulation frequency. Each pixel is approximately 20 μm. Inset shows the normalized profiles highlighting a broader peak width for the 0.2 Hz measurement. (b) Signal intensity over modulation frequencies from 0.02–2 Hz at 4.4 mA/cm^2 for a defect in a different Li/β-Li$_3$PS$_4$/Li cell.

to the control, even at ∼40 times lower nominal current density per contact area. We attribute the greater signal magnitude in the post-breakdown cells to increased resistive heat generation at the smaller-area dendrites where the actual current densities may be relatively high.

Importantly, the dendrites likely follow circuitous or branching paths though the pelletized electrolyte, although the heat signatures that we measure in the Li/β-Li$_3$PS$_4$/Li cells appear point-like under our measurement conditions. The point-like features that we observe may indicate either that the horizontal span of the dendrite is smaller than our ∼20 μm spatial resolution, or that we primarily detect heat at the top point of the dendrite where it contacts the electrode rather than detecting vertical heat diffusion through the electrolyte from the underlying complex dendrite structure. We illustrate the latter possibility as a cartoon in Figure 4g, where the dendrite could have a relatively large sub-surface horizontal span, though heat may reach the surface mainly through the dendrite's thermally-conductive lithium pathways, after which the heat would symmetrically diffuse from the top point of the dendrite horizontally along the lithium electrode disk. Indeed, our scanning electron microscopy results in Figure 4h indicate that the electrolyte's pore structure spans 10's to 100's of micrometers, suggesting that the sub-surface dendrite structure could be larger than the hot spots that we detect in our thermal images.

We note that using a slower modulation frequency of 0.2 Hz (Figures 4b, 4d) compared to 2 Hz (Figures 4a, 4c) provides higher signal magnitude at the expense of slightly lower spatial resolution. We highlight this effect in Figure 5a by overlaying line scans through the upper left defect in Figures 4a–4b. For this defect, we observe almost double signal magnitude at 0.2 Hz compared to 2 Hz. The normalized line scans also show a relatively stronger diffuse heat background for the 0.2 Hz measurement, although the full-width-at-half-max of the point-like heat signature increases only slightly.

We attribute the more diffuse heat signal at 0.2 Hz to heat diffusion farther away from the point of generation within this longer modulation period. Heat diffusion — and thus the extended halo around

the heat source that decreases signal resolution — is proportional to the thermal diffusion length, $\Lambda = \sqrt{\alpha/\pi f}$, where α is thermal diffusivity and f is the modulation frequency.[23] In addition, at slower modulation frequencies it is possible that that vertical heat diffusion through the electrolyte from sub-surface dendrite heating contributes more strongly to the image, similarly giving rise to a diffuse heat background.

In Figure 5b, we use a breakdown site from another representative Li/β-Li$_3$PS$_4$/Li cell to show that the signal amplitude continues to increase with decreasing modulation frequencies and plateaus at slow frequencies (<0.05 Hz). While most breakdown sites that we have measured follow this general trend, we note that the strength of modulation dependence may vary for defects with different geometries, even within the same sample. In particular, the trend of increasing amplitude with decreasing modulation frequency is expected to be pronounced for extended heat sources but minimal for near-surface point-like heat sources due to differences in the oscillating surface power density of thermal waves originating at differently shaped objects.[23,29] For this reason, the geometry and depth of the heat sources affects the optimal modulation frequency to simultaneously detect multiple defects, obtain high signal magnitude, and maintain minimal compromise of resolution.

We further discuss the origin of this frequency dependence in Figure 6 by presenting the oscillating heat signal over time with respect to the current stimulus. Here, we show that the sample's thermal relaxation time also contributes to the modulation frequency dependence of the signal amplitude. In short, we show that the signal is maximized when the modulation frequency becomes slower than the sample's thermal relaxation time, although additional factors beyond the sample's internal thermal properties (i.e. heat exchange to the surroundings) become important at very slow modulation frequencies.

In Figure 6, we compare the oscillating heat signal for a Li/β-Li$_3$PS$_4$/Li cell modulated at 0.01 Hz (Figure 6a) with the more straightforward example of a resistor modulated between 0.01–1 Hz (Figures 6b–6c). The heat signal in the Li/β-Li$_3$PS$_4$/Li cell gradually increases over time, with periodic fluctuations matching the current modulation frequency. The modulated signal represents heat generation at a breakdown site, and we attribute the gradual heating to poor heat sinking. As shown quantitatively by Breitenstein and coworkers, the peak-to-peak height of the frequency-dependent signal defines the spatially varying heat signatures, while the gradual temperature drift over the course of the measurement results in a constant offset in the total image amplitude.[23] The gradual change in the temperature background should not significantly affect our qualitative ability to locate breakdown sites, although better heat sinking would nevertheless improve defect detection by increasing the peak-to-peak difference in the modulated signal.

In Figures 6b–6c, we illustrate how the signal amplitude at a given modulation frequency depends on the sample's thermal relaxation time using the example of a resistor. The lock-in detected heat amplitude is given by the difference in signal over the modulation period, which is maximized when the sample dissipates all heat within the period. For example, at a slow frequency of 0.01 Hz, Figure 6b shows that the resistor fully cools to its original temperature before the next resistive heating cycle. In this case, frequencies slower than 0.01 Hz would not significantly increase the magnitude of modulated heat. For the Li/β-Li$_3$PS$_4$/Li cells, this explains the plateau in signal magnitude below 0.05 Hz in Figure 5b. Figures 6c and 6d show that the modulated amplitude decreases with increasing frequency, since the sample cannot fully dissipate all heat within the modulation period.

Importantly, the slowest modulation frequency is not necessarily the optimal modulation frequency, despite the increase in lock-in detected amplitude at slow frequencies with complete heat dissipation. In addition to the decrease in resolution at slow frequencies, the impact of heat exchange to the surroundings becomes increasingly important, making the measurement more sensitive to external factors such as heat sinking. As shown in Figures 6b–6d, the 0.01 Hz measurement captures complete heat exchange with the surroundings whereas the 1 Hz measurement does not, although the average equilibrated
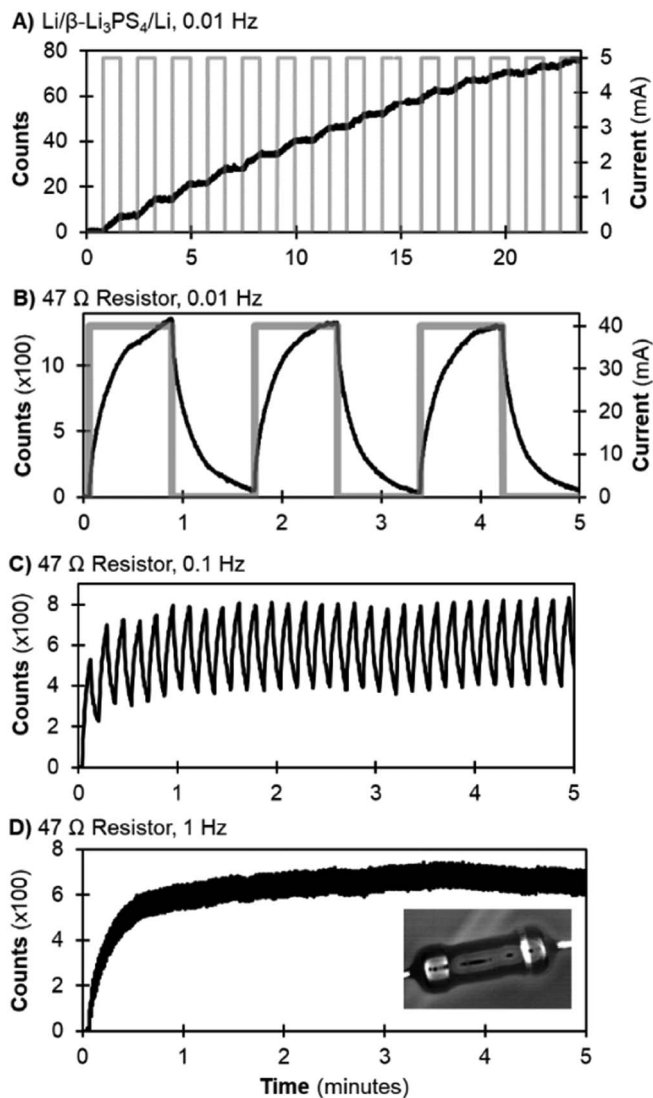

Figure 6. Detector counts (black trace, left axis) along with modulated current amplitude (gray trace, right axis) for (a) Li/β-Li$_3$PS$_4$/Li at 0.01 Hz with 5 mA max amplitude and for (b-c) a 47 Ω resistor at 0.01, 0.1, and 1 Hz with 40 mA max amplitude. Inset shows a steady-state image of the resistor recorded on the thermal camera.

temperature is independent of modulation frequency for a given current density. At the faster frequencies, the sample approaches a quasi-adiabatic (heat-insulated) state in which the modulated heat profile only depends on the sample's internal thermal properties.[23]

We note that testing a range of modulation frequencies may provide useful information about the materials under study, such as the depth and geometry heat sources,[29] heat resistance to the surroundings for a given cell construction, and internal thermal parameters such as heat capacity (from $\alpha = k/(\rho \, x \, c_p)$, where k is the thermal conductivity, ρ is density, and c_p is heat capacity). Very recently, frequency-dependent thermal imaging has been applied to silicon solar cells for "3D analysis" of cell breakdown.[29] We propose that frequency-dependent thermal measurements may similarly become a powerful tool for characterizing new battery materials and cell structures as a more detailed understanding of the systems' transient thermal responses is developed.

Improving cell design based on lock-in thermography images.— We next show an example in which we applied lock-in thermography to improve our Li/β-Li$_3$PS$_4$/Li cell design. In our early design, the
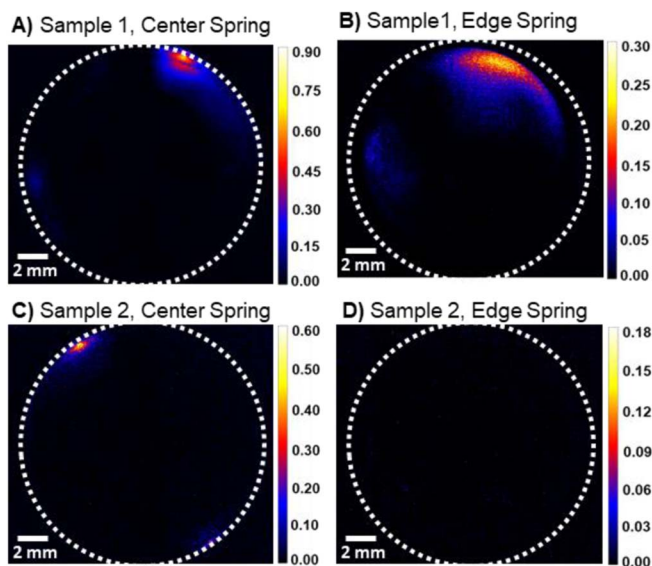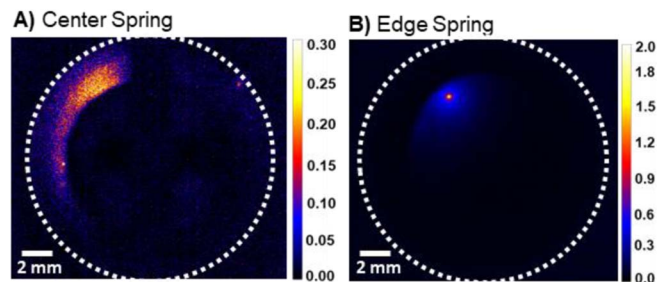
Figure 7. Thermal images of two Li/β-Li$_3$PS$_4$/Li cells with lithium electrodes that extend to the sample edges, imaged using a spring that covers either (a,c) the sample center or (b,d) the sample edges, showing that breakdown sites occur at the cell edges. Images were collected using lock-in detection referenced to a current modulated at 0.2 Hz at a max amplitude of 1.8 mA/cm^2. Dotted line indicates the edge of the pelletization die, just outside the β-Li$_3$PS$_4$/die interface. Intensity scale is given as detector counts.

lithium electrodes cover the entire β-Li$_3$PS$_4$ surface and contact the inside of the pelletization die. Using lock-in thermal imaging, we show post-breakdown heating at the sample edges, likely due to dendrite growth at the interface between the β-Li$_3$PS$_4$ pellet and the die. Guided by the thermal images, we eliminate β-Li$_3$PS$_4$/die interface dendrites by preventing lithium contact with the pelletization die in our new cell design.

Figure 7 shows post-breakdown thermal images of two representative cells fabricated with our old design. We image the cells using the two different spring structures shown in Figures 1b–1c in order to view defects at the cell edges (Figures 7a, 7c) or center (Figures 7b, 7d). For reference, we draw a circle around the edge of the pelletization die where the sample contacts the die. Figure 7a gives the edge view of Sample 1, showing a point-like heat signature in the upper right at the β-Li$_3$PS$_4$/die interface as well as a weaker diffuse heat signature in the lower left region away from the interface. Figure 7b shows the center view of the same sample. From the center view, we observe diffuse heat in the upper right, corresponding to the extended halo around the point-like edge defect. In the lower left, we find that the diffuse heat signature in the interior region of the cell is maximized at about 1.5 mm from the edge of the die, at a location that is blocked by the center spring in Figure 7a. In Figure 7c, we show two similar point-like edge defects in Sample 2. By observing the center view (Figure 7d), we show that there is minimal sample breakdown in the cell's interior region.

Our observation of breakdown primarily at the β-Li$_3$PS$_4$/die interfaces in our old cell design suggests that the weak points around the sample perimeter limited the cell's performance. Importantly, these weak points also limited our ability to test the robustness of our battery materials. That is, the β-Li$_3$PS$_4$/die interface is not part of the final battery, so breakdown at this interface provides no useful information about the path forward for improving our materials.

In order to test our active materials rather than being limited by the β-Li$_3$PS$_4$/die interfaces, we modified our cell design to prevent the lithium electrodes from contacting the die. Figure 8 shows representative thermal images of our next generation cell design, where the lithium contacts are smaller (~1.5 cm^2 vs. 2.0 cm^2) and do not reach the die interface. With this new design, Figure 8a shows that

Figure 8. Thermal images of a Li/β-Li$_3$PS$_4$/Li cell with centered lithium electrodes that do not reach the sample edges imaged using a spring that covers (a) the sample center or (b) the sample edges, showing that breakdown can no longer occur at the sample edge. Images were collected using lock-in detection referenced to a current modulated at 0.2 Hz at a max amplitude of 2.7 mA/cm^2. Intensity scale is given as detector counts.

breakdown cannot occur at the cell edges. In Figure 8a, we observe a weak diffuse heat signature extending from a point blocked by the center spring. In Figure 8b, we show that the point-like heat signature is within the cell interior, ~3.5 mm away from the sample edge. Such heat signatures at the cell interior are more representative of the actual defect sites and failure mechanisms that would occur in a real battery device, enabling future characterization of the local structural and compositional properties that correlate with breakdown of solid-state electrolytes.

Conclusions

In this study, we showed that lock-in thermal imaging is an effective technique for evaluating new electrochemical materials and for optimizing test structures to appropriately assess the relevant defects and failure mechanisms. To enable widespread application of lock-in thermography to battery systems, we discussed several critical parameters necessary to optimize this technique. We showed the importance of employing strategies to increase and homogenize surface thermal emissivity, such as using black paint on a top foil contact. In addition, we highlighted the balance between the material's thermal relaxation time and lock-in modulation frequency. We showed that slow modulation frequencies maximize signal amplitude, but that complete thermal relaxation comes with additional challenges such as decreased resolution and a larger impact of heat exchange to the surroundings. As an example, we applied lock-in thermography to image dendritic defect sites in symmetric Li/β-Li$_3$PS$_4$/Li cells after breakdown. We showed that our old cell design limited our ability to test our active materials because breakdown occurred primarily at the unimportant β-Li$_3$PS$_4$/die interfaces. Therefore, we improved our cell design to ensure that breakdown is associated instead with our battery-relevant materials and interfaces. We note that, in this study, we used lock-in thermography to iteratively improve our cell design by locating the cell's problem areas after breakdown has occurred, and subsequently fabricating cells that do not contain such problem areas. However, we propose that this technique could also be used to locate inhomogeneous heating prior to breakdown, allowing one to study the nature of pre-breakdown hot spots that may accelerate lithium propagation and eventually cause cell breakdown. Our study provides an important example of how lock-in thermography can inform the targeted optimization of next-generation battery materials and cell designs.

Acknowledgments

ORCID

Dana B. Sulas https://orcid.org/0000-0003-0814-8723
Natalie Seitzman https://orcid.org/0000-0001-8901-6751

References

1. K. Fu, Y. Gong, B. Liu, Y. Zhu, S. Xu, Y. Yao, W. Luo, C. Wang, S. D. Lacey, J. Dai, Y. Chen, Y. Mo, E. Wachsman, and L. Hu, "Toward Garnet Electrolyte–Based Li Metal Batteries: An Ultrathin, Highly Effective, Artificial Solid-State Electrolyte/Metallic Li Interface," *Sci. Adv.*, **3**, e1601659 (2017).
2. K. Kerman, A. Luntz, V. Viswanathan, Y.-M. Chiang, and Z. Chen, "Review—Practical Challenges Hindering the Development of Solid State Li Ion Batteries," *J. Electrochem. Soc.*, **164**, A1731 (2017).
3. T. M. Bandhauer, S. Garimella, and T. F. Fuller, "A Critical Review of Thermal Issues in Lithium-Ion Batteries," *J. Electrochem. Soc.*, **158**, R1 (2011).
4. K. E. Thomas and J. Newman, "Thermal Modeling of Porous Insertion Electrodes," *J. Electrochem. Soc.*, **150**, A176 (2003).
5. C. F. Lopez, J. A. Jeevarajan, and P. P. Mukherjee, "Experimental Analysis of Thermal Runaway and Propagation in Lithium-Ion Battery Modules," *J. Electrochem. Soc.*, **162**, A1905 (2015).
6. D. P. Finegan, M. Scheel, J. B. Robinson, B. Tjaden, I. Hunt, T. J. Mason, J. Millichamp, M. Di Michiel, G. J. Offer, G. Hinds, D. J. L. Brett, and P. R. Shearing, "In-Operando High-Speed Tomography of Lithium-Ion Batteries During Thermal Runaway," *Nat. Commun.*, **6**, 6924 (2015).
7. S. Panchal, I. Dincer, M. Agelin-Chaab, R. Fraser, and M. Fowler, "Transient Electrochemical Heat Transfer Modeling and Experimental Validation of a Large Sized LiFePO$_4$ /Graphite Battery," *Int. J. Heat Mass Transfer*, **109**, 1239 (2017).
8. M. Streza, C. Nuţ, C. Tudoran, V. Bunea, A. Calborean, and C. Morari, "Distribution of Current in the Electrodes of Lead-Acid Batteries: A Thermographic Analysis Approach," *J. Phys. D: Appl. Phys.*, **49**, 055503 (2016).
9. R. R. Richardson, P. T. Ireland, and D. A. Howey, "Battery Internal Temperature Estimation by Combined Impedance and Surface Temperature Measurement," *J. Power Sources*, **265**, 254 (2014).
10. R. R. Richardson and D. A. Howey, "Sensorless Battery Internal Temperature Estimation Using a Kalman Filter with Impedance Measurement," *IEEE Trans. Sustain. Energy*, **6**, 1190 (2015).
11. H. P. G. J. Beelen, L. H. J. Raijmakers, M. C. F. Donkers, P. H. L. Notten, and H. J. Bergveld, "An Improved Impedance-Based Temperature Estimation Method for Li-Ion Batteries," *IFAC-PapersOnLine*, **48**, 383 (2015).
12. Y. Kim, S. Mohan, J. B. Siegel, A. G. Stefanopoulou, and Y. Ding, "The Estimation of Temperature Distribution in Cylindrical Battery Cells under Unknown Cooling Conditions," *IEEE Trans. Control Sys. Technol.*, **22**, 2277 (2014).
13. C. Forgez, D. Vinh Do, G. Friedrich, M. Morcrette, and C. Delacourt, "Thermal Modeling of a Cylindrical LiFePO$_4$/Graphite Lithium-Ion Battery," *J. Power Sources*, **195**, 2961 (2010).
14. M. S. K. Mutyala, J. Zhao, J. Li, H. Pan, C. Yuan, and X. Li, "In-Situ Temperature Measurement in Lithium Ion Battery by Transferable Flexible Thin Film Thermocouples," *J. Power Sources*, **260**, 43 (2014).
15. L. H. J. Raijmakers, D. L. Danilov, J. P. M. van Lammeren, M. J. G. Lammers, and P. H. L. Notten, "Sensorless Battery Temperature Measurements Based on Electrochemical Impedance Spectroscopy," *J. Power Sources*, **247**, 539 (2014).
16. J. P. Schmidt, S. Arnold, A. Loges, D. Werner, T. Wetzel, and E. Ivers-Tiffée, "Measurement of the Internal Cell Temperature Via Impedance: Evaluation and Application of a New Method," *J. Power Sources*, **243**, 110 (2013).
17. Z.-J. Wang, Z.-Q. Li, and Q. Liu, "Infrared Thermography Non-Destructive Evaluation of Lithium-Ion Battery." In *Proc. of SPIE*, **8193**, 81934I (2011).
18. Z. Li, J. Zhang, B. Wu, J. Huang, Z. Nie, Y. Sun, F. An, and N. Wu, "Examining Temporal and Spatial Variations of Internal Temperature in Large-Format Laminated Battery with Embedded Thermocouples," *J. Power Sources*, **241**, 536 (2013).
19. C.-Y. Lee, S.-J. Lee, Y.-M. Hung, C.-T. Hsieh, Y.-M. Chang, Y.-T. Huang, and J.-T. Lin, "Integrated Microsensor for Real-Time Microscopic Monitoring of Local Temperature, Voltage and Current inside Lithium Ion Battery," *Sens. Actuators, A*, **253**, 59 (2017).
20. B. J. Robinson, R. P. Shearing, and J. D. Brett, "Thermal Imaging of Electrochemical Power Systems: A Review," *J. Imaging*, **2**, 2 (2016).
21. J. B. Robinson, J. A. Darr, D. S. Eastwood, G. Hinds, P. D. Lee, P. R. Shearing, O. O. Taiwo, and D. J. L. Brett, "Non-Uniform Temperature Distribution in Li-Ion Batteries During Discharge – a Combined Thermal Imaging, X-Ray Micro-Tomography and Electrochemical Impedance Approach," *J. Power Sources*, **252**, 51 (2014).
22. J. B. Robinson, E. Engebretsen, D. P. Finegan, J. Darr, G. Hinds, P. R. Shearing, and D. J. L. Brett, "Detection of Internal Defects in Lithium-Ion Batteries Using Lock-in Thermography," *ECS Electrochem. Lett.*, **4**, A106 (2015).
23. O. Breitenstein, W. Wilhelm, and M. Langenkamp, *Lock-in Thermography*, Second ed.; Springer-Verlag: Berlin Heidelberg (2010).
24. M. Nagao, A. Hayashi, M. Tatsumisago, T. Kanetsuku, T. Tsuda, and S. Kuwabata, "In Situ SEM Study of a Lithium Deposition and Dissolution Mechanism in a Bulk-Type Solid-State Cell with a Li2S–P2S5 Solid Electrolyte," *PCCP*, **15**, 18600 (2013).
25. R. Garcia-Mendez, F. Mizuno, R. Zhang, T. S. Arthur, and J. Sakamoto, "Effect of Processing Conditions of 75Li2S-25P2S5 Solid Electrolyte on Its DC Electrochemical Behavior," *Electrochim. Acta*, **237**, 144 (2017).
26. F. Han, J. Yue, X. Zhu, and C. Wang, "Suppressing Li Dendrite Formation in Li2S-P2S5 Solid Electrolyte by LiI Incorporation," *Adv. Energy Mater.*, **8**, (2018).
27. L. Porz, T. Swamy, B. W. Sheldon, D. Rettenwander, T. Frömling, H. L. Thaman, S. Berendts, R. Uecker, W. C. Carter, and Y.-M. Chiang, "Mechanism of Lithium Metal Penetration through Inorganic Solid Electrolytes," *Adv. Energy Mater.*, **7**, 1701003 (2017).
28. T. Yamada, S. Ito, R. Omoda, T. Watanabe, Y. Aihara, M. Agostini, U. Ulissi, J. Hassoun, and B. Scrosati, "All Solid-State Lithium–Sulfur Battery Using a Glass-Type P2S5–Li2S Electrolyte: Benefits on Anode Kinetics," *J. Electrochem. Soc.*, **162**, A646 (2015).
29. O. Breitenstein, H. Straube, and K. Iwig, "Lock-in Thermography with Depth Resolution on Silicon Solar Cells," *Sol. Energy Mater. Sol. Cells*, **185**, 66 (2018).